Proceedings of Global Power and Propulsion Society
ISSN-Nr: 2504-4400
GPPS Montreal26
September 9-11, 2026
www.gpps.global

GPPS-TC-2026-0178

PREDICTION OF TRAILING EDGE WALL-PRESSURE FLUCTUATIONS IN ROTOR CONFIGURATIONS WITH NEURAL OPERATORS

Jean Fesquet
DAEP, ISAE-SUPAERO
jean.fesquet@isae-supaero.fr
Toulouse, France

Antonio Alguacil
Université de Sherbrooke
antonio.alguacil.cabrerizo@usherbrooke.ca
Sherbrooke, QC, Canada

Yannick Bousquet
DAEP, ISAE-SUPAERO
yannick.bousquet@isae-supaero.fr
Toulouse, France

Marlène Sanjosé
École de Technologie Supérieure
marlene.sanjose@etsmtl.ca
Montréal, QC, Canada

Stéphane Moreau
Université de Sherbrooke
stephane.smoreau@gmail.com
Sherbrooke, QC, Canada

Michaël Bauerheim
DAEP, ISAE-SUPAERO
michael.bauerheim@isae-supaero.fr
Toulouse, France

Nicolas Binder
DAEP, ISAE-SUPAERO
nicolas.binder@isae-supaero.fr
Toulouse, France

ABSTRACT

Rapid prediction methods to evaluate rotor self-noise can rely on turbulent boundary layer parameters extracted from Reynolds-Averaged Navier-Stokes (RANS) simulations, from which wall-pressure fluctuation spectra (WPS), the main noise sources, are reconstructed with models. An acoustic analogy then provides the far-field noise. To yield an efficient pipeline inside an aero-acoustic optimization framework over a large range of geometries, a recent state-of-the-art neural operator model (MARIO) that was shown to learn realistic turbomachinery flow fields is coupled with recently developed neural networks based either on Gene-Expressing Programming or an Autoencoder chained with a fully-connected Neural Network. MARIO has been retrained on RANS simulations of a mixed flow fan configuration at several operating conditions. MARIO is shown to accurately predict boundary layer parameters for wall-pressure spectra predictions. The newly developed MARIO+WPS pipeline has been successfully validated with accurate wall-pressure spectra extracted from a Large Eddy Simulation (LES) of the same configuration. Predictions of far-field noise based on Amiet's approach and the newly developed data-driven WPS have also been shown to provide reliable estimates when compared with far-field noise obtained from LES using the Ffowcs Williams and Hawkings acoustic analogy.

INTRODUCTION

Modern turbofan engines achieve higher efficiency thanks to increased bypass ratios using a larger fan diameter. This results in larger fan blade heights and chord length, which have a strong effect on the rotor noise mechanisms, namely tip gap and trailing-edge noise (TEN) due to the scattering of turbulent boundary layers at trailing edges. While the effect of these rotor noise sources was traditionally masked in the overall noise signature by the dominant rotor-stator interaction noise, their relative importance is increasing in modern ultra-high bypass ratio engines. Here, the objective is to model the rotor-alone trailing-edge noise at high speeds.

Rapid prediction methods to evaluate TEN are typically based on a three-step approach: first, turbulent boundary layer parameters are extracted from Reynolds-Averaged Navier-Stokes (RANS) simulations. Then, unsteady wall-pressure fluctuation spectra (WPS) are estimated with models, the latest of which employ neural networks Arroyo Ramo et al. (2026) for

This work is licensed under **Attribution-NonCommercial-NoDerivatives 4.0 International (CC-BY-NC-ND)**
See: https://creativecommons.org/licenses/by-nc-nd/4.0/legalcode

improved predictions in low-speed turbomachinery Zhou et al. (2025). Finally, these are fed into an unsteady aerodynamic response model, followed by an acoustic analogy to calculate the far-field noise. Nonetheless, the need to perform RANS simulations hinders the efficient use of such a pipeline inside an aeroacoustic optimization loop. Furthermore, the new WPS models have not yet been tested in high-speed configurations. Consequently, the main objective of this paper is to introduce and evaluate a novel pipeline that couples both RANS and WPS models using deep learning networks.

Recent state-of-the-art neural operator models have been able to learn realistic flow fields (Catalani et al., 2025), including 3D turbomachinery flows over a large range of geometries (Fesquet et al., 2025). These neural operators provide an efficient framework since they are (i) fully differentiable, (ii) resolution invariant, (iii) can be trained by sub-sampling the initial mesh to avoid memory issues, and finally (iv) can be inferred at local query points, avoiding the extraction of full 3D flows when only local profiles or probes are required. Here, the objective is to show that such neural operators can be used for both aerodynamic predictions and providing the necessary input for aeroacoustic predictions, i.e., to accurately predict the boundary layer parameters for wall-pressure spectra to evaluate TEN. The whole pipeline will be evaluated against the WPS obtained by Large Eddy Simulations (LES).

In this study, we choose the neural operator model MARIO. It has been retrained to capture the turbulent boundary layer quantities, based on RANS simulations of a mixed flow fan at several operating conditions, representative of turbo-engine applications. The methodology of the MARIO+WPS pipeline is described in the next section. Results of the RANS simulations, MARIO predictions, and the wall-resolved LES of the ducted fan are then compared. Finally, MARIO is used to extract the relevant inputs for a network-based WPS model. Predicted WPS is then validated with the wall-pressure spectra extracted from the LES. Evaluations of errors and their impact on the TEN broadband noise are finally assessed to conclude.

METHODOLOGY

The pipeline, including MARIO for the reconstructed flow field around a typical turbomachinery stage and fast analytical/neural network-based models of WPS, is first described. The test case selected for application, is a mixed flow fan, shown in Fig. 1, which is typical of aircraft Heat and Ventilation Air-Conditioning (HVAC) systems. The constant duct radius is denoted by R_d, the nominal rotating speed of the fan by Ω_n, the blade count by B. The blade passing frequency (BPF) is defined as $B\Omega_n$.

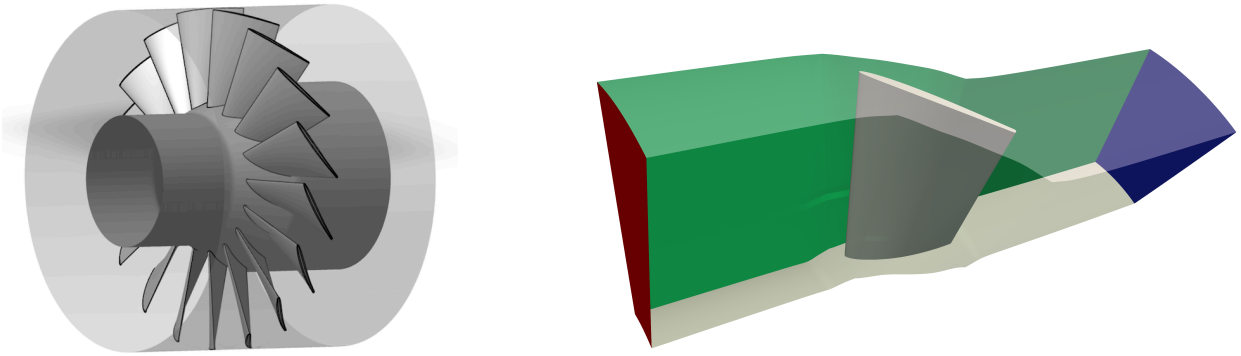


Figure 1 Investigated fan and computational domain.

Surrogate modelling - MARIO

The neural operator model MARIO (Modulated Aerodynamic Resolution Invariant Operator) introduced by Catalani et al. (2025) combines operator learning (Kovachki et al., 2023) objectives with a neural-field (or implicit neural representation (Sitzmann et al., 2020)) formulation to achieve state-of-the-art performance demonstrated on the AirfRANS dataset, for instance (Yagoubi et al., 2025). It also leverages resolution independence to enable training from a subsampled set of mesh points and inference at arbitrary spatial locations, reducing memory requirements compared with graph-based approaches and enabling scalability to large CFD meshes such as those built for turbomachinery stages.

Neural fields learn the mapping between arbitrary spatial locations and any field values of interest φ. In the context of MARIO, multiple mappings depending on parameters μ, representing geometry or operating conditions, can be learned at once via the use of FiLM conditioning (Perez et al., 2018), where a hyper-network (Fig. 2 (b)) modulates the weights of the main network (Fig. 2 (a)). With m representing MARIO, an inference with the trained model at location $\mathbf{X}$ can be written in the following way: $m_\mu(\mathbf{X}) = \hat{\varphi}_{\mu,\mathbf{X}} \approx \varphi_{\mu,\mathbf{X}}$, where μ is passed into the hyper-network for modulation. For the sake of simplicity, here the geometry is fixed during the study. Thus, μ corresponds only to the operating point. It is worth noting that variable geometry datasets can be learnt with a similar approach, where a latent representation of the geometry is concatenated within μ, as demonstrated by Catalani et al. (2025).

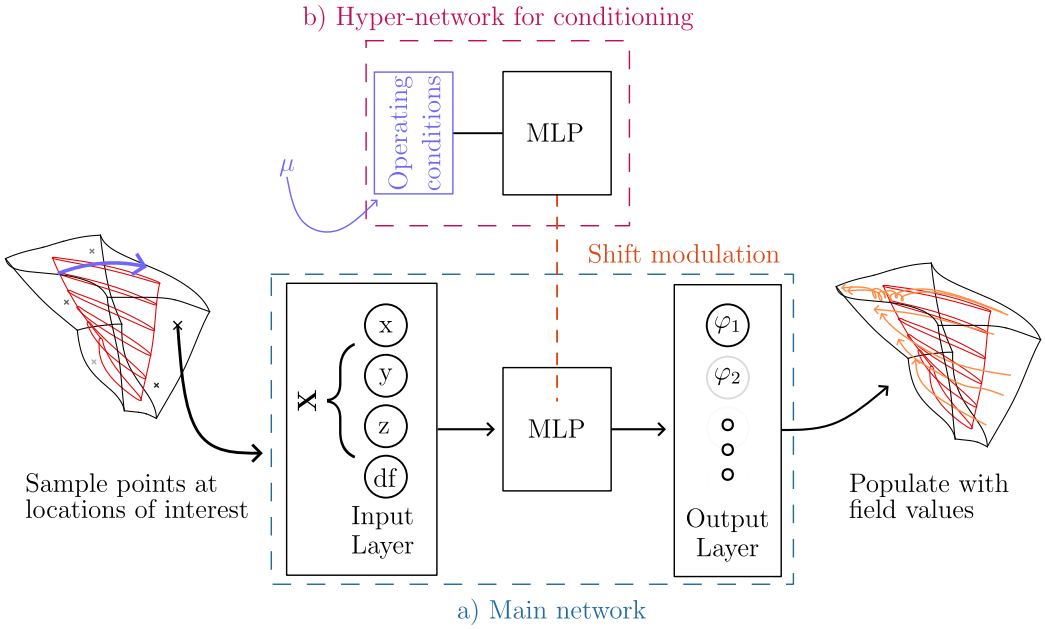


Figure 2 Sketch of the MARIO architecture with the main MLP network (a) and its modulation by the hyper-network (b) for conditioning by the operating conditions μ. The 3D Cartesian coordinates are fed as inputs of the main network, along with the signed distance function to the wall (e.g., blade, hub, or shroud), denoted *df*. The main network outputs field value at the corresponding coordinate $\varphi(x,y,z)$.

Since the network produces point-wise predictions, the training process can rely on aggressive subsampling of the spatial domain to ensure both computational efficiency and scalability to large meshes. In practice, good performance can be achieved with extreme subsampling ratios. Here, 20k points out of the 2.4M original mesh points are used per iteration, corresponding to a subsampling ratio of 0.8%. To ensure the proper coverage of the full spatial domain, these points are randomly resampled at each training iteration. This stochastic sampling strategy allows the model to progressively explore the entire field while maintaining a manageable computational cost. This also provides a key advantage at inference time: the model represents the full 3D volume as a continuous function, allowing predictions of the field values at any cherry-picked location. For example, this enables targeted evaluations at some specific regions of interest, such as along blade normals to extract boundary layer profiles, without requiring the evaluation of the entire domain as with graph neural networks, thereby drastically reducing the inference computational cost.

In practice, the training of MARIO requires approximately $\sim$ 30 minutes on a single *NVidia A100* GPU, which corresponds roughly to the time needed to compute a single operating point using RANS on 24 CPU cores. Inference is significantly faster, especially for targeted inquiries such as surface extraction or probe evaluation: predicting 10k points takes around 30 milliseconds. This speed-up allows near real-time interactivity with the model, making the approach well-suited for iterative design exploration. This highlights the main strength of MARIO: a lightweight and fast architecture. The presented results were achieved with a main network composed of 6 layers of 512 neurons and the hyper-network with 4 in depth and 256 in width. This MARIO architecture has been specifically designed to be sample-efficient, enabling training on small datasets: typical orders of magnitude are a few hundred samples for varying geometries, and considerably fewer for the fixed geometry considered here. Its accuracy on turbomachinery flows has been quantified elsewhere: on a full 3D compressor map of the DGEN-380 fan rotor (6.4M points per sample, transonic operating points), MARIO recovers integrated quantities post-processed from the predicted fields with a 1.16% mean error on isentropic efficiency, comparable to a dedicated MLP scalar regressor (2.28%), and locates shocks with a mean offset of 1.73% of chord on unseen operating points (Fesquet et al., 2026). It has likewise been benchmarked on public datasets with geometric variability (Catalani et al., 2025; Yagoubi et al., 2025). Building on this established generalisation capability, the present paper deliberately focuses on a single geometry: the objective is to demonstrate and validate the complete pipeline, from the reconstructed 3D flow field to the far-field acoustic prediction, against a wall-resolved LES, a reference only affordable for one configuration. After training, MARIO within the proposed framework can be used for joint aerodynamic-acoustic optimisation or rapid screening of relevant configurations.

Amiet's approach for fan self-noise

The rotor self-noise is computed using Amiet's approach (Amiet, 1989). The rotor is divided into 10 uncorrelated strips, with blade-to-blade correlation being neglected. The blade chunks are considered as isolated airfoils in rotation, which can

be modeled as an infinite sum of rectilinear translations (Sinayoko et al., 2013). At each angular position, Amiet's trailing-edge noise model for a finite-chord flat plate (Roger and Moreau, 2005; Lee et al., 2021) is applied, accounting for the Doppler frequency shift caused by the moving blade chunks relative to the fixed observers (Amiet, 1989; Sinayoko et al., 2013). The model computes the airfoil response to turbulent gusts scattering at the trailing edge and its back-scattering at the leading-edge. Far-field noise is obtained analytically using Curle's analogy, assuming infinite span and free-field propagation (Roger and Moreau, 2005). The approach requires few geometrical and flow parameters for each blade chunk, and a statistical description of the turbulent gusts produced by the boundary layers developing along the blades (Lee et al., 2021). The frozen turbulence scattering at the trailing edge is described with a wall pressure fluctuation spectrum and a correlation length at a location close to the trailing-edge. In the present study, the classical Corcos's correlation model was used (Corcos, 1964) and several WPS models were evaluated. Sound power levels (SWL) are computed from the surface integration of the sound pressure level computed on a sphere of radius $R = 10R_d$ centered on the fan. This approach has been successfully used on various rotor geometries (Sanjosé and Moreau, 2018; Zhou et al., 2025; Santamaria et al., 2026).

Wall Pressure Spectrum Models

This study evaluates three models for the power spectral density (PSD) of the wall-pressure fluctuations are evaluated as input for noise predictions based on Amiet's approach, described previously. The models, dubbed "Lee 2018", "GEP 2023" and "ANN 2025", define the WPS from a set of boundary layer flow quantities that can be obtained in RANS simulations. Their key characteristics are summarized below.

"Lee 2018" model is a semi-empirical model built on preceding work by Rozenberg et al. (2012) who modified the functional form of Goody's model to include the effect of adverse pressure gradients (APG). Lee's improvements include functional exponents that are calibrated on a larger experimental database for both low and high pressure gradient flows (Lee, 2018). The model was tested and validated on data at Reynolds numbers based on the boundary-layer momentum thickness θ, Re_θ, within the range $1.4\times10^3 < Re_\theta < 2.34\times10^4$ for zero pressure-gradient flows and within the range $0.5\times10^3 < Re_\theta < 1.65\times10^4$ for APG flows, with a maximum Clauser parameter $\beta_c = (\theta/\tau_w)(dp/dx)$ of 28.57. Lee's model is given by the equation

$$\frac{\phi_{pp}U_e}{\tau_w^2\delta^*} = \frac{\left[\max\left(a,(0.25\beta_c-0.52)\,a\right)\right]\widetilde{\omega}^2}{\left[4.76\widetilde{\omega}^{0.75}+d^*\right]^e+\left[C_3\widetilde{\omega}\right]^{h^*}} \tag{1}$$

where $\tilde{\omega} = \frac{\omega\delta^*}{U_e}$. τ_w is the wall shear stress, δ^* the boundary-layer displacement thickness and U_e the external velocity. The definition of the other constants in this model is given in (Lee, 2018; Lee et al., 2021).

"GEP 2023" model is a data-driven extension of semi-empirical models of WPS. It consists of the selection of the most suitable function using a Gene Expression Programming (GEP) evolutionary algorithm to fit input data built from a set of chosen physical variables and constants over a large experimental database informed from RANS boundary layer predictions and direct numerical simulation data of a CD airfoil (Wu et al., 2020) to address performance issues at high pressure gradients (Fritsch et al., 2023; Shubham et al., 2024). The model used here (GEP-A in (Shubham et al., 2024)) is given by:

$$\frac{\phi_{pp}U_e}{Q^2\theta} = \frac{C_f\left(\bar{f}_1\right)^{1.29}+\Delta^{(-G-2.23)}\bar{f}_1^{-0.096}}{\left[3.02R_T^{0.178}\bar{f}_2\right]^{1.92H}+\left[7.96G-C_f-3.78\bar{f}_1^{-0.96}\right]5.23\beta_{c4}} \tag{2}$$

where $Q = \frac{1}{2}\rho U_e^2$, $\Delta = \delta/\delta^*$, $H = \delta^*/\theta$, $\beta_{c4} = (\delta/Q)(dp/dx)$, $C_f = \tau_w/Q$, $G = \sqrt{\left(2.0/C_f\right)}(1-1/H)$, $\overline{f_1} = \frac{\delta}{U_e}f$ and $\overline{f_2} = \frac{\theta}{U_e}f$. Δ stands for Zagarola-Smit's parameter, and H for the shape factor. δ is the boundary-layer thickness. Note that β_{c4} is a modified Clauser's parameter that does not involve the wall shear stress.

"ANN 2025" is a machine learning-based model that leaverages the interpretability capabilities of artificial neural network (ANN) to identify the dependencies between boundary layer properties and the associated WPS. To mitigate the high variability and over-fitting risks inherent in such an approach, "ANN 2025" employs a two-step strategy proposed by Arroyo Ramo et al. (2026). The first step consists of finding a low-dimensional representation of the time-averaged local boundary layer profiles: the tangential velocity profile extracted along surface normals, $U_t/U_\infty(h/c)$, at fixed chordwise position x/c is provided to a neural network autoencoder. This autoencoder compresses the boundary layer into a three-dimensional latent space, from which it is possible to reconstruct the full boundary layer velocity profile.

The second step consists of passing these three latent space parameters L_1, L_2, and L_3, together with the airfoil (or blade strip) Reynolds number, Re_c based on the upstream velocity U_∞ and the chord length, x/c, the location along the chord where the wall-pressure spectra has to be evaluated, and a vector of Strouhal numbers, $St = fc/U_\infty$, where the WPS has to be evaluated. This results in the following functional form for the predicted normalized WPS (Zhou et al., 2025):

$$\frac{\phi_{pp}U_\infty}{Q_\infty^2 c} = g(L_1, L_2, L_3, Re_c, x/c, St), \tag{3}$$

where $Q_\infty = \frac{1}{2}\rho U_\infty^2$. Contrary to semi-empirical, GEP, or other neural network WPS models (Dominique et al., 2022), this approach is able, in principle, to consider any type of two-dimensional boundary layer profile, including laminar or turbulent separated regions, since it does not require calculating integral boundary layer parameters. Nonetheless, the capacity to capture such phenomena is dependent on the quality of the training database. Here, the ANN is trained on a database of Large Eddy Simulations and Direct Numerical Simulations, accounting for Reynolds numbers based on the chord in the range of 1.5×10^5 to 2.4×10^6 and Mach numbers from 0.25 to 0.7. Note also that these training simulations contain examples of laminar separation bubbles but not of turbulent separations, since the angles of attack are kept below 8°. More details on the training technique and database can be found in Arroyo Ramo et al. (2026) and Zhou et al. (2025)

RANS AND LES RESULTS

Two different numerical approaches were set up in this study. The training of the flow-predicting surrogate requires multiple operating points to be run. Therefore, the RANS approach is used as a fast flow simulation method to construct a dataset and as a basis to obtain the post-processed acoustic quantities. To validate the obtained quantities, a wall-resolved LES is also performed.

RANS setup

The computational domain encompasses a single blade passage with 2.5 blade chord lengths upstream and 3 blade chord lengths downstream, shown in Figure 1 (right). The mesh is a multi-block structured O-6H mesh built with Cadence Autogrid5. The size of the first cell at walls is defined to achieve dimensionless distances to the wall y^+ below 1 in all turbulent parts of the blades. The grid has about 2.4 million points. The RANS equations are solved with FINE/Turbo v18 from Cadence. Turbulent flow is modelled with the k–ω SST turbulence model and the Langtry and Menter transition model (Langtry and Menter, 2009). Preliminary numerical tests have shown that this combination of models provides the closest results to the LES boundary layer profiles. In terms of boundary conditions, a rotational periodicity is imposed on azimuthal boundaries (shown in green in Fig. 1). The walls are adiabatic, and a no-slip condition is applied. At the inlet of the calculation domain (shown in red), the total pressure, the total temperature, and the flow angle ($\alpha = 0$) are imposed while a mass flow condition is set at the outlet (in blue) to control the operating point. Each computation took approximately 12 CPU-Hours to converge, and 63 operating points have been run over four iso-RPM lines (50%, 75%, 100%, and 125% of the nominal rotational speeds).

LES setup

For the wall-resolved large eddy simulation, the numerical domain (single blade passage) and the mesh topology (multi-block structured O-6H mesh) are identical to those described above for the RANS simulations. The size of the first cell at the walls is maintained at $3\mu m$, ensuring a $y+$ value close to 1. However, to satisfy the mesh resolution criteria reported in the literature for wall-resolved LES: $50 < \Delta s^+ < 150$, $15 < \Delta r^+ < 40$; the mesh has been significantly refined, resulting in approximately 210 million grid points. The wall-resolved large eddy simulation is performed using the *elsA* solver developed by ONERA. As for the RANS simulations, spatial periodicity is imposed at the azimuthal boundaries, while adiabatic no-slip conditions are applied at the walls. At the inlet of the calculation domain, the total pressure, total temperature, and flow angle ($\alpha = 0$) are imposed. The operating point is controlled by imposing the static pressure at the outlet. Since no non-reflecting boundary condition is used, the outlet boundary is shifted downstream, and the mesh is progressively coarsened when approaching the outlet. Time integration is carried out using a second-order implicit Gear scheme, with local convergence of sub-iterations using a Newton algorithm. A maximum of 5 sub-iterations is needed to decrease by two orders of magnitude the residuals in the inner loop. The convective fluxes are computed with a third-order upwind scheme. A single rotor rotation is described with 12000 time-steps. Finally, turbulence closure at the subgrid scale is provided by the Wall-Adapting Local Eddy-Viscosity (WALE) model.

Figure 3 presents the time-averaged (left) axial velocity fields extracted at mid-span. Velocities are made dimensionless using the reference velocity $U = \Omega_n R_d$. The simulated operating point corresponds to a higher mass flow rate than the nominal operating point. Therefore, the rotor blades operate under a slight negative incidence angle, with the stagnation point located on the pressure side. A boundary layer separation occurs on the pressure side at approximately 25% of the blade chord, triggering transition to the turbulent state as identified by the Q criterion shown in Figure 3 (center). On the suction side, a similar boundary layer separation is observed at 90% of the blade chord, which also induces boundary layer transition clearly identified by the high levels of pressure fluctuations in Figure 3 (right). Pressure fluctuations are made dimensionless by the reference dynamic pressure $Q_\infty = 1/2\rho U^2$. The boundary layer quantities required to inform the WPS models described previously were extracted at three chordwise positions x/C close to the trailing edge as identified by the dots in Figure 3 (right). The tip of the blade is influenced by the tip leakage flow interaction, especially the rear blade corner, where high-pressure fluctuations can be seen.

The unsteady wall pressure was recorded with a high sampling frequency of 80 BPF on the blade for one revolution. The pressure time series extracted at the locations identified in Fig. 3 (right) are used to compute reference spectra for evaluating the three WPS models. In addition, the blade surface pressure supports the computation of far-field acoustics by

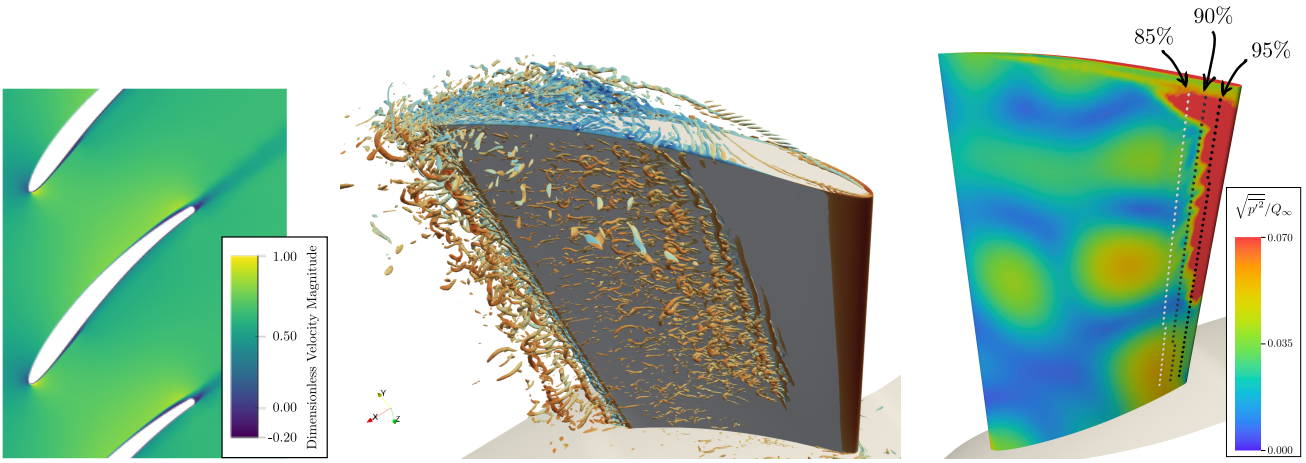


Figure 3 Time-averaged axial velocity field extracted at mid-span (left), instantaneous iso-surface of Q criterion seen from the blade pressure side (middle), and root-mean-square of the pressure on the suction side of the blade (right). The dots identify the location of the boundary layer extractions.

means of the Ffowcs Williams and Hawkings (FWH) analogy which, like Amiet's approach, assumes free-field acoustic propagation. In the present work, the pressure collected on the solid surfaces serves as input for the in-house SherFWH code, which implements the advanced time formulation proposed by Casalino (2003).

Dataset and learning task

The dataset was composed of multiple operating points run with the RANS setup described earlier. The samples were split randomly into training and validation sets, in addition to one part being omitted from the training set to test the robustness of the model, as seen in Fig. 4. This led to a 66-33 train-validation split. Gaps in the dataset can be observed on each iso-line as the global quantities failed to converge in these regions, although convergence had previously been achieved when not employing a transition model. While the number of samples is small, good performance was achieved on the dataset thanks to the limited variability in the flow over the various samples.

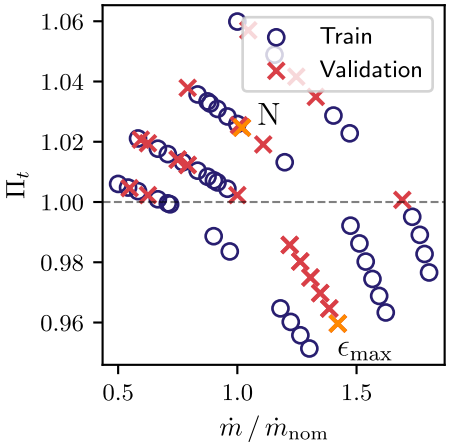


Figure 4 Total pressure ratio Π_t as a function of the mass flow rate normalised with the nominal mass flow rate for all the RANS points. The nominal operating point is marked with N and the sample leading to the highest error is denoted $\varepsilon_{\max}$.

The learning task completed by the model was to learn the three velocity components, along with the temperature, pressure, and density, from the boundary conditions μ (rotational speed and static pressure at the outlet) and the spatial locations and distance function $\mathbf{X}$. The distance function used in this case is the "turbulent distance" output by the solver, which serves for turbulence modelling. Adding the field as input has been observed to improve the results, even in this fixed geometry context.

RESULTS AND DISCUSSION

Field predictions with MARIO

Figure 5 demonstrates the surrogate model's capacity to learn the dataset by comparing axial velocity contours $0.1c$ downstream of the trailing edge. The top row illustrates the sample with the maximum prediction error ($\epsilon_{\max}$), which corresponds to an operating point near the choke limit (wind-milling, Fig. 4) characterized by severe pressure-side stall across more than 50% of the span. For context, the two nearest training samples, corresponding to the maximum $\dot{m}$ points on the 50% and 100% nominal RPM Ω_n lines, are shown with identical color scaling. A localized high-error region is visible downstream of the tip gap, peaking at a 25% relative error against the RANS mean cut velocity. Although significant, this error is concentrated in an area dominated by tip clearance vortices, known for its highly sensitive physics. Because of the restricted spatial extent, this local discrepancy does not significantly impact the post-processed radial distributions. From now on, we focus on the 100% nominal RPM line for the consequent acoustic analysis.

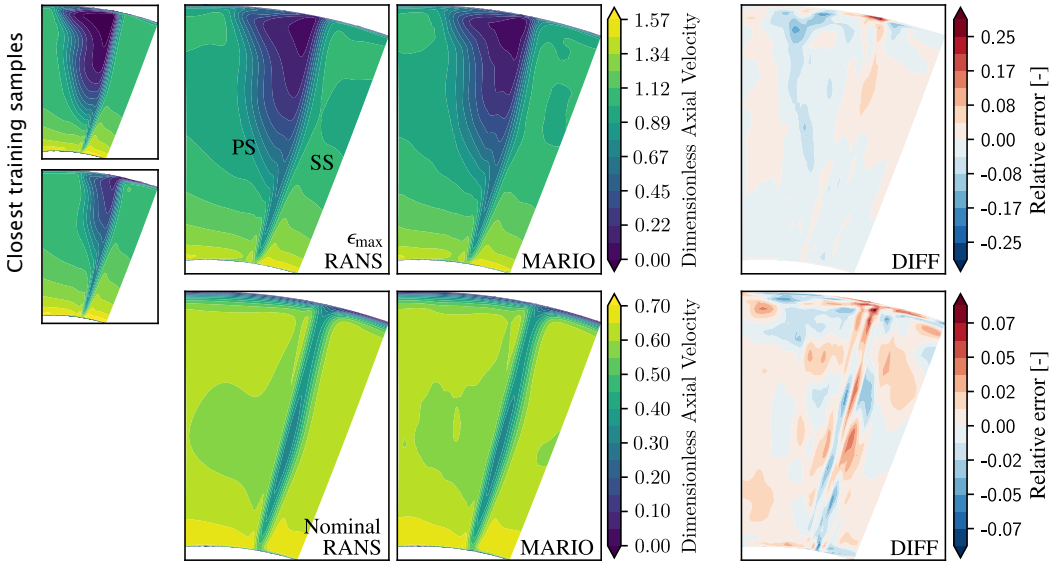


Figure 5 Axial contour of axial velocity 0.1c aft of the trailing edge. Top is the highest error sample, and bottom is the nominal operating point. The blade rotates counter-clockwise, the pressure-side PS is upstream to the left, and the suction-side SS is upstream to the right. Velocity are made dimensionless by $R_d\Omega_n$.

Figure 6 first shows the spanwise variation of the physical boundary layer parameters extracted from the above reconstructed RANS simulations at the nominal flow conditions, on the suction side of the blade, and at three locations near the trailing edge (85%, 90% and 95% of the chord, respectively, see Figure 3). Very similar trends are observed at the three extraction points. The Zagarola-Smit's parameter Δ substantially varies along the span with thicker boundary layer parameters at the hub and at the tip because of low Reynolds numbers and stronger adverse pressure gradients, respectively. The shape factors H are greater than 2 and quasi-uniform along the blade span: this confirms the transitional state of the boundary layer as already seen in the Q-criterion in Fig. 3. Clauser's parameter β_c has the largest variations, with values reaching up to 50. This signals the presence of a very strong adverse pressure gradient near the trailing edge. The Reynolds number Re_θ also evidences the significant growth of the boundary layer near the trailing edge. Figure 6 also provides the corresponding three latent space variables deduced from the autoencoder in the "ANN 2025" methodology described above, applied to the full mean velocity profiles extracted at the same three chordwise locations. Very similar profiles along the span are seen for the three parameters, with more variations on the second variable, L_2, according to the extraction point.

Wall-pressure spectra

From the parameters extracted in Fig. 6 and the WPS models described above, the PSD of the wall-pressure fluctuations that represent the noise sources statistics for trailing-edge noise can be reconstructed along the blade span at the extraction point. Figure 7 shows the corresponding predictions at 50, 75, and 90% span. For comparison between spectral amplitude estimated at various span locations, the WPS scaling uses $U_\infty \equiv \Omega_n R_d$ in Fig. 7. The WPS is also computed from the wall-pressure time history measured at the same locations in the LES. Note that no substantial differences have been found between the direct RANS inputs and the reconstructed ones with MARIO (the latter being obtained instantaneously from the ANN). The state-of-the-art semi-empirical model (Lee, 2018) significantly underpredicts the LES levels as found before on the NASA-SDT turbofan configuration (Sanjosé et al., 2019) and on the EDAT helicopter tail-rotor configuration (Zhou et al., 2025), whereas both the "GEP 2023" and the "ANN 2025" match them more closely. Interestingly, at the extraction point closer to the trailing edge, where the flow is more turbulent, the ANN outperforms all other models in terms of levels.

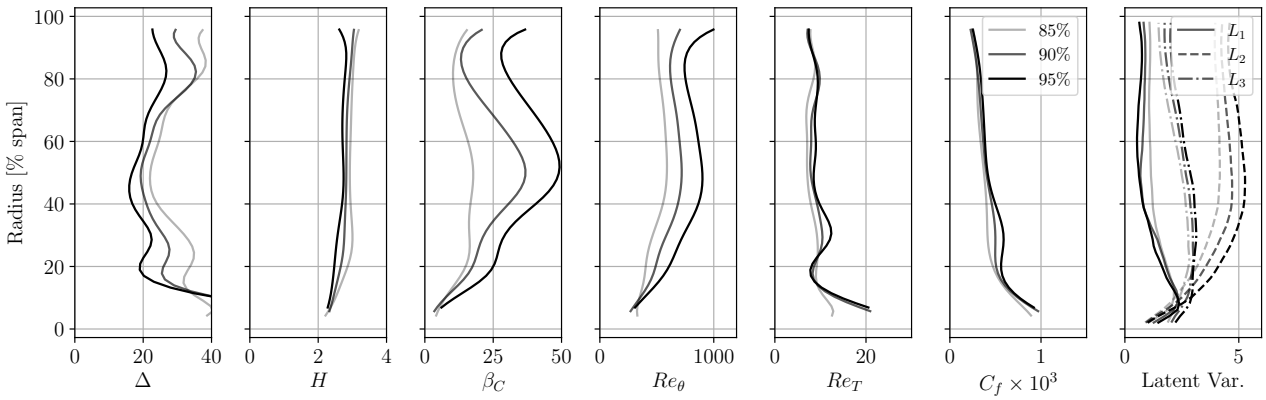


Figure 6 Radial variation of physical boundary layer parameters and latent space values with RANS inputs along the radius, extracted at 85%, 90% and 95% of the chord

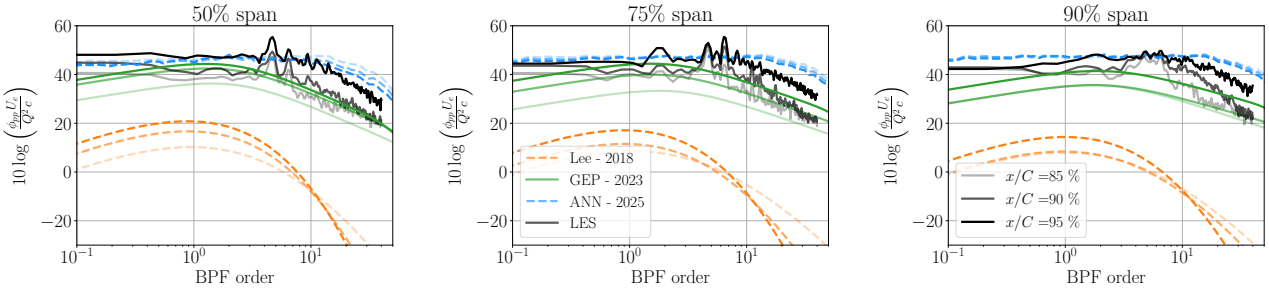


Figure 7 Power spectral densities of the wall-pressure fluctuations at 50%, 75%, and 90% span at different extraction locations near the trailing edge.

The LES spectrum shows tonal content, which is typical of the transition mechanisms occurring at the extraction location. The "Lee 2018" and the "GEP 2023" models predict a roll-off location at 2 BPF approximately, while the "ANN 2025" one is at 10 BPF within better agreement to the roll-off from the LES spectra. Regarding high-frequency decay, "Lee 2018" model largely overpredicts the slope, "GEP 2023" slightly underpredicts it, while "ANN 2025" provides the best agreement. Compared to other models, the "ANN 2025" model shows little to no sensitivity to the extraction location.

Far-field acoustics

The sound power levels computed using Amiet's approach and the three WPS models is compared with the reference LES in Fig. 8. Similarly to the spectral content shown in Fig. 7, the LES spectra shows a hump between BPF order 1.5 and 10 corresponding to the laminar boundary layer instability noise captured and low to moderate Reynolds number (Sanjose et al., 2019; Santamaria et al., 2026). This mechanisms is evenmore visible in the far-field noise spectra due the strong correlation of the shedded vortical structures (Sanjose et al., 2019). This mechanism is not considered in the present broadband noise analytical models. Noise prediction obtained with the WPS predicted with "Lee 2018" model underestimates the SWL by more than 30 dB. Similar discrepancies with Rozenberg's model were obtained on the SDT benchmark (Sanjosé et al., 2019). Both the "ANN 2025" and the "GEP 2023" models provide more accurate noise levels within 10 dB of the reference LES. These results are consistent with recent works (Shubham et al., 2023; Zhou et al., 2025) and demonstrate that data-driven WPS models can improve noise predictions. Models based on physical parameters of the boundary layer are very sensitive to the extraction location, showing a spread of 10 dB in the predicted SWL values. On the contrary, the "ANN 2025" model is totally blind to the extraction location and provides more robust noise prediction. With the LES results as reference, the "ANN 2025" outperforms the other models in terms of amplitude.

CONCLUSIONS

The wall-pressure spectra and trailing-edge broadband noise of the mixed flow fan have been investigated by analytical and data-driven approaches extracted from either Reynolds Averaged Navier-Stokes simulations or the MARIO neural operator surrogate, which accurately reproduces the same time-averaged quantities as the RANS baseline. An additional wall-resolved Large Eddy Simulation has been carried out at the nominal design point, serving for validation purposes.

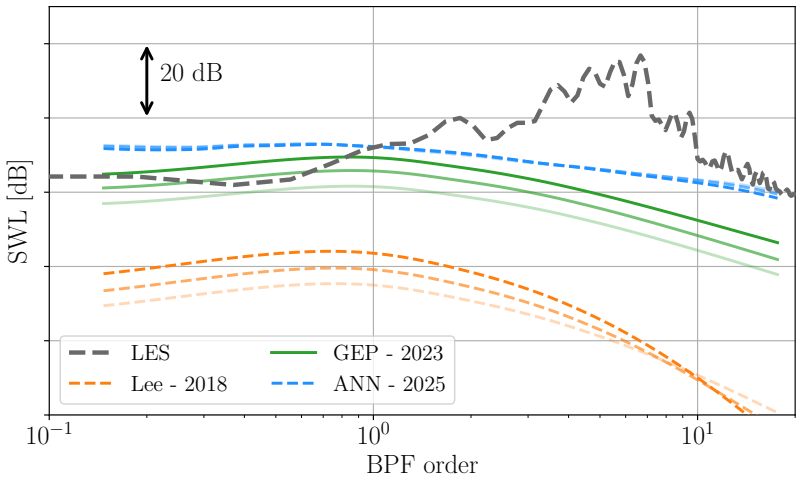


Figure 8 Sound power levels from reference LES and Amiet's approach using WPS extracted at different locations near the trailing edge.

A database of RANS simulations at varying operating conditions has been generated, helping train the neural operator. Results show that the operator can accurately predict the averaged quantities, even at off-design conditions.

The present demonstration is restricted to a single geometry and to interpolation within the sampled operating envelope; extension of the pipeline to variable geometries, together with the corresponding LES validation of the boundary-layer parameters and of the wall-pressure spectra, is left to future work.

RANS or MARIO boundary layer parameters close to the blade trailing edge can then be extracted to inform different models that predict the wall-pressure fluctuations spectra. Three approaches have been tested: classical semi-empirical models, symbolic data-driven models (GEP), and artificial neural networks (ANN) trained on high-fidelity airfoil simulations. Comparisons with the wall-pressure spectra extracted from the reference LES show that both GEP and ANN are significantly more accurate than classical models. The GEP predictions remain sensitive to the choice of the location of the extractions along the chord. The ANN model outperforms the other evaluated models in terms of roll-off location and high frequency spectral decay of the WPS.

Finally, the sound power level of the full machine is calculated, comparing LES results with Amiet's model informed by the different WPS models. Theses results confirm the predictive accuracy of GEP and ANN approaches, being in a band of ± 10 dB around the reference LES values. The ANN model provides a more robust prediction without sensitivity to the location of the extraction.

In the future, both neural network surrogates, namely the flow predictor (MARIO) and the unsteady pressure spectra predictor ("ANN 2025"), could be fully coupled to leverage their end-to-end differentiability. This would enable their use inside optimization loops or as quick pre-design tools, studying the sensitivity of aerodynamics and aeroacoustics to changes in geometry or flow conditions.

ACKNOWLEDGMENTS

This research project is partially funded by the "Agence de l'Innovation de Defense" (AID) and by the Natural Sciences and Engineering Research Council of Canada (Discovery Grants RGPIN-2020-05919 and RGPIN-2019-05844). The authors acknowledge the partners of the UHEQ Consortium, which develops and provides the acoustic software PyFanNoise for this research. Post-processing was enabled in part by means of the Antares Python API developed by CERFACS, and was carried out on the Trillium supercomputer administered by the Digital Research Alliance of Canada.

REFERENCES

Amiet, R. K. (1989), *Noise produced by turbulent flow into a rotor: theory manual for noise calculation*, National Aeronautics and Space Administration, Langley Research Center.

Arroyo Ramo, A., Alguacil, A., Bauerheim, M., Moreau, S. and Jacob, M. C. (2026), 'Artificial Neural Networks Prediction of Wall-Pressure Spectrum: A Boundary-Layer Insight', *AIAA Journal* **In Press**, 1–19.

Casalino, D. (2003), 'An advanced time approach for acoustic analogy predictions', *Journal of Sound and Vibration* **261**(4), 583–612.

Catalani, G., Fesquet, J., Bertrand, X., Tost, F., Bauerheim, M. and Morlier, J. (2025), 'Towards scalable surrogate models based on Neural Fields for large scale aerodynamic simulations', *Computers & Fluids* p. 106929.
URL: *https://www.sciencedirect.com/science/article/pii/S0045793025003895*

Corcos, G. M. (1964), 'The structure of the turbulent pressure field in boundary-layer flows', *Journal of Fluid Mechanics* **18**(3), 353–378.

Dominique, J., Van den Berghe, J., Schram, C. and Mendez, M. A. (2022), 'Artificial neural networks modeling of wall pressure spectra beneath turbulent boundary layers', *Physics of Fluids* **34**(3), 035119.

Fesquet, J., Bauerheim, M. and Binder, N. (2026), Assessment of a Full-Field Neural Surrogate (mario) for Turbomachinery Flow Applications, *in* 'ASME Turbo Expo 2026: Turbomachinery Technical Conference and Exposition', American Society of Mechanical Engineers, Milan, Italy, pp. GT2026–177674.

Fesquet, J., Bauerheim, M., Rojda, L., Bousquet, Y. and Binder, N. (2025), 'Application of Deep Learning for Fan Rotor Blade Performance Prediction in Turbomachinery', *Journal of Turbomachinery* **147**(111002).

Fritsch, D. J., Vishwanathan, V., Roy, C. J., Todd Lowe, K., Devenport, W. J., Croaker, P., Tkachenko, O., Pook, D., Lane, G., Shubham, S. and Sandberg, R. D. (2023), 'Modeling the Surface Pressure Spectrum Beneath Turbulent Boundary Layers in Pressure Gradients', *AIAA Journal* **61**(5), 2002–2021.

Kovachki, N., Li, Z., Liu, B., Azizzadenesheli, K., Bhattacharya, K., Stuart, A. and Anandkumar, A. (2023), 'Neural Operator: Learning Maps Between Function Spaces With Applications to PDEs', *Journal of Machine Learning Research* **24**(89), 1–97.
URL: *http://jmlr.org/papers/v24/21-1524.html*

Langtry, R. B. and Menter, F. R. (2009), 'Correlation-Based Transition Modeling for Unstructured Parallelized Computational Fluid Dynamics Codes', *AIAA Journal* **47**(12), 2894–2906.
URL: *https://arc.aiaa.org/doi/10.2514/1.42362*

Lee, S. (2018), 'Empirical wall-pressure spectral modeling for zero and adverse pressure gradient flows', *AIAA Journal* **56**(5), 1818–1829.

Lee, S., Ayton, L., Bertagnolio, F., Moreau, S., Chong, T. P. and Joseph, P. (2021), 'Turbulent boundary layer trailing-edge noise: Theory, computation, experiment, and application', *Progress in Aerospace Sciences* **126**, 100737.

Perez, E., Strub, F., de Vries, H., Dumoulin, V. and Courville, A. (2018), 'FiLM: Visual Reasoning with a General Conditioning Layer', *Proceedings of the AAAI Conference on Artificial Intelligence* **32**(1).
URL: *https://ojs.aaai.org/index.php/AAAI/article/view/11671*

Roger, M. and Moreau, S. (2005), 'Back-scattering correction and further extensions of Amiet's trailing-edge noise model. Part 1: Theory', *Journal of Sound and Vibration* **286**(3), 477–506.

Rozenberg, Y., Robert, G. and Moreau, S. (2012), 'Wall-Pressure Spectral Model Including the Adverse Pressure Gradient Effects', *AIAA Journal* **50**(10), 2168–2179.

Sanjosé, M. and Moreau, S. (2018), 'Fast and accurate analytical modeling of broadband noise for a low-speed fan', *The Journal of the Acoustical Society of America* **143**(5), 3103–3113.

Sanjose, M., Towne, A., Jaiswal, P., Moreau, S., Lele, S. and Mann, A. (2019), 'Modal analysis of the laminar boundary layer instability and tonal noise of an airfoil at Reynolds number 150,000', *International Journal of Aeroacoustics* **18**(2-3), 317–350.

Sanjosé, M., Kholodov, P., Perez-Arroyo, C. and Moreau, S. (2019), Cfd modeling of a realistic turbofan blade for noise prediction. part 2: Analytical acoustic predictions, *in* 'Proceedings of Global Power and Propulsion Society (GPPS 2019)', Beijing, China, pp. GPPS–BJ–2019–224.

Santamaria, J., Belliot, S., Sanjosé, M., Gojon, R. and Moreau, S. (2026), 'Serration manufacturing effects on propeller trailing edge noise mechanisms', *Journal of Sound and Vibration* **626**, 119656.

Shubham, S., Pargal, S., Moreau, S., Sandberg, R. D., Yuan, J., Kushari, A. and Sanjose, M. (2023), Data-driven empirical wall pressure spectrum models for fan noise prediction, *in* 'AIAA AVIATION 2023 Forum', p. 3508.

Shubham, S., Sandberg, R. D. and Kushari, A. (2024), 'More General Wall Pressure Spectra Models: Combining Feature Engineering with Evolutionary Algorithms', *AIAA Journal* **62**(7), 2622–2637.

Sinayoko, S., Kingan, M. and Agarwal, A. (2013), 'Trailing edge noise theory for rotating blades in uniform flow', *Proceedings of the Royal Society A: Mathematical, Physical and Engineering Sciences* **469**(2157), 20130065.

Sitzmann, V., Martel, J. N. P., Bergman, A. W., Lindell, D. B. and Wetzstein, G. (2020), Implicit neural representations with periodic activation functions, *in* 'Proceedings of the 34th International Conference on Neural Information Processing Systems', NIPS '20, Curran Associates Inc., Red Hook, NY, USA, pp. 7462–7473.
URL: *https://dl.acm.org/doi/10.5555/3495724.3496350*

Wu, H., Moreau, S. and Sandberg, R. D. (2020), 'On the noise generated by a controlled-diffusion aerofoil at Rec=150,000', *Journal of Sound and Vibration* **487**, 115620.

Yagoubi, M., Danan, D., Leyli-Abadi, M., Mazari, A., Brunet, J.-P., Kabalan, A., Casenave, F., Ma, Y., Catalani, G., Fesquet, J., Helwig, J., Zhang, X., Yu, H., Bertrand, X., Tost, F., Baurheim, M., Morlier, J. and Ji, S. (2025), 'NeurIPS 2024 ML4CFD Competition: Results and Retrospective Analysis'.
URL: *http://arxiv.org/abs/2506.08516*

Zhou, Z., Arroyo, A., Pouhe Hiol, R. K., Pargal, S., Sanjosé, M. and Moreau, S. (2025), Data-driven wall pressure spectrum models for fan noise prediction, *in* 'International Conference on Fan Noise, Aerodynamics, Applications and Systems (Fan 2025)', Antibes – Juan-les-Pins, France, pp. 243–252.